Simultaneous measurements of freestream disturbances, boundary layer instabilities, and transition location on sharp and blunt cones in hypersonic flow

Andrew P. Ceruzzi*, Laurent M. Le Page†, Philipp Kerth‡, Benjamin A.O. Williams§, and Matthew McGilvray¶
Oxford Thermofluids Institute, University of Oxford, Oxford, OX2 0ES, United Kingdom

Boundary layer instabilities and transition to turbulence on a 7-degree half-angle cone with varying nose-tip radii in Mach 6 and 7 flow are investigated using a combination of surface heat transfer measurements, surface pressure measurements, and high speed schlieren images. The experiments are performed at unit-Reynolds numbers ranging from $[22-44]\times 10^6/\mathrm{m}$ in University of Oxford's High-Density Tunnel (HDT). The transition Reynolds number, Re_{X_T}, increases with increasing nose tip Reynolds number, Re_{R_N}, for $Re_{R_N} \leq 10^5$. In this range, evidence of second-mode wave instabilities are observed in both schlieren images and surface pressure measurements. For $10^5 < Re_{R_N} < 4\times 10^5$, Re_{X_T} remains constant and coherent streaks above the boundary layer are observed with schlieren imaging. Images of the interaction of these features with a boundary layer breaking down to a fully turbulent state are presented. The freestream disturbance environment is also varied through existence of several steady state plateaus created by the natural operation of the facility, and characterised with multi-point focused laser differential interferometry (FLDI). Re_{X_T} increases by $\sim 10-60\%$ with increasing plateau number which is independent of Re_{R_N}. Variation in freestream fluctuation amplitude with frequency and Reynolds number are in agreement with previous studies while variation with plateau is not. The discrepancy is explained by receptivity functions which are sensitive to the inclination angle of disturbances. A method for measuring the inclination angle using correlated FLDI signals is presented and reveals a consistent trend with plateau number. The trend is physically explained by changes in the relative contribution of entropic and acoustic modes with time.

I. Nomenclature

a	=	speed of sound
c_p	=	specific heat capacity
f	=	frequency
H_w	=	FLDI beam radius transfer function
$\vec{k}$	=	disturbance wave-vector
L_{SR}	=	integration length
M	=	Mach number
M_r	=	relative Mach number
P	=	pressure
$\dot{q}$	=	heat flux
r	=	recovery factor
R_{ij}	=	cross-correlation
Re	=	Reynolds number
R_N	=	nose radius
St	=	Stanton number

*Postdoctoral Research Assistant, Department of Engineering Science, University of Oxford, AIAA Member
†Senior Postdoctoral Researcher, Department of Engineering Science, University of Oxford
‡D.Phil. University of Oxford
§Assoc. Professor, Department of Engineering Science, University of Oxford
¶Professor, Department of Engineering Science, University of Oxford

t = time from tunnel start-up
T = temperature
U, u = streamwise velocity
u_c = streamwise convection velocity
v_c = spanwise convection velocity
V = voltage
w_0 = beam radius parameter at focus
x = streamwise distance from sharp nose tip
X_s = surface coordinate from stagnation point
y = vertical spanwise coordinate
Y_s = wall normal coordinate
z = horizontal spanwise coordinate / optical axis
γ = ratio of specific heats
δ = boundary layer thickness
Δt = time difference
Δx_1 = intra-probe spacing
Δx_2 = streamwise inter-probe spacing
Δy_2 = spanwise inter-probe spacing
$\Delta \phi$ = phase difference
θ_c = cone half-angle
θ_n = inclination angle of disturbance
λ_0 = laser wavelength
ρ = density
τ = sample time period

Subscripts

0 = stagnation/plenum condition
∞ = freestream condition
e = boundary layer edge condition
$fill$ = barrel condition
ij = between probe/channel i and probe/channel j
w = wall condition

Acronyms

FLDI = Focused Laser Differential Interferometry
FOV = field-of-view
HDT = Oxford's High Density Tunnel
PSD = power spectral density
TFG = Thin Film Gauge

II. Introduction

One of the largest challenges facing designers of hypersonic vehicles is predicting the location of laminar to turbulent boundary layer transition on the surface of the vehicle [1]. In hypersonic boundary layers, transition to turbulence is associated with significant increases in skin friction and heat transfer [2], which in turn affects predictions of drag, engine inlet conditions, and thermal protection requirements. Uncertainty in the location of transition leads to over-designed thermal protection systems and unpredictable performance.

The boundary layer transition process can be categorized into three parts: (1) laminar boundary layer receptivity to freestream disturbances, (2) growth of instabilities inside the boundary layer, and (3) breakdown of a transitioning boundary layer to fully turbulent flow [3]. Freestream disturbance levels have a significant influence on the location of transition [4] and vary widely between facilities [5]. Thus, a proper transition study requires accurate measurements of freestream noise at frequencies corresponding to the relevant instabilities in the boundary layer [6]. For sharp, slender cones at zero angle-of-attack in hypervelocity flow ($M_\infty > 4$), the dominant instability is the Mack, or second mode [7]. This mode, a trapped acoustic wave in the boundary layer, can exhibit frequencies in excess of $100kHz$ [7]. Thus, high temporal resolution measurement techniques are required to resolve these waves as well as the freestream disturbances which seed their initial amplitudes [8, 9].

As nose radius (R_N) increases, the size of the entropy layer increases in turn stabilizing the second mode [10]. This causes the transition front to move downstream with increasing bluntness until a critical Reynolds number ($Re_{R_N} \sim 10^6$) at which point this trend reverses [11]. Beyond the critical range, the dominant transition mechanism is believed to be roughness near the stagnation point [3, 12–14]. For 'moderately blunt' nose tips near or below the critical range, the mechanisms that lead to transition are less well understood and the subject of many recent works [15–17]. Stetson et al. [18] were the first to report hot wire measurements of unstable disturbances above the boundary layer, but inside the entropy layer for an 8-degree half-angle cone in Mach 8, $Re_{unit} = 8.2 \times 10^6$/m flow with nose tip radii ranging from $[4 - 18]mm$. They hypothesized that these disturbances in the entropy layer could excite instabilities in the boundary layer as the entropy layer is swallowed by the boundary layer. Downstream from here, amplification and breakdown of the second mode would lead to transition, just as with the sharp nose case. Maslov et al. [19] conducted similar experiments on a 7-degree cone in Mach 6, $Re_{unit} = [12.2 – 22.6] \times 10^6/m$ flow with $2mm$ and $20mm$ nose tip radii. They observed weak fluctuations in the entropy layer with hot-wires, casting doubt on the previous hypothesis. More recently, Grossir et al. [15] reported laser induced fluorescence (LIF) illuminated schlieren images of sweeping, wisp-like disturbances above the boundary layer on 7-degree cone in Mach 11.8, $Re_{unit} = [11 - 12] \times 10^6$/m flow with a $4.75mm$ nose tip. Simultaneously, surface mounted PCB sensors measured a dominant disturbance frequency consistent with the second mode. Paredes et al. [16, 20] provided a comprehensive investigation of nose bluntness effects on transition over slender cones through both wind tunnel experiments, theoretical and computational fluid dynamics (CFD) analysis. Some relevant conclusions include: (1) nose bluntness stabilizes the second mode, (2) transition-reversal in the critical range cannot be explained by linear stability theory (LST), and (3) a transient growth analysis reveals significant amplification of non-modal, travelling planar waves above the boundary layer but inside the entropy layer. The authors suggested an investigation of receptivity and the effect of freestream noise on the disturbances in the entropy layer as useful follow-on work. Kennedy et al. [17] characterized non-modal features in the entropy layer above a 7-degree cone in Mach 6, $Re_{unit} = [18 - 23] \times 10^6$/m flow with a $5.08mm$ nose tip using high-speed schlieren visualizations and surface pressure transducers. Notably, they identified high-frequency pressure signals coincident with the trailing edge of the non-modal wisp-like features. They also recommended freestream characterization as important future work, as well as direct observation of the breakdown of the non-modal features to turbulence.

The objectives of this work are to:

1) examine the effects of nose-bluntness and freestream disturbances on instabilities and transition location along a slender, asymmetric body in hypersonic flow,
2) investigate the connections, if any, between non-modal, entropy layer instabilities and second mode waves,
3) observe the breakdown to turbulence of these non-modal entropy layer features,
4) comprehensively characterize the freestream disturbance environment upstream of these instabilities.

These objectives are accomplished with an experimental campaign in University of Oxford's High Density Tunnel (HDT), a heated Ludwieg tube capable of freestream Mach numbers up to 7 and unit Reynolds numbers greater than 40×10^6/m [21]. The model of study is a 7-degree half-angle cone instrumented with surface pressure sensors, thin film heat transfer gauges (TFGs), and an interchangeable nose tip [22, 23]. The start of transition is experimentally determined from the TFGs, the boundary and entropy layer flow-field is interrogated with high-speed schlieren visualizations, and the freestream disturbance environment is characterized with multi-point focused laser differential interferometry (FLDI) [8, 24–29].

III. Facility, model, and instrumentation

A schematic of Oxford's High Density Tunnel (HDT) operating as a Ludwieg Tube [21] is provided in Fig.1, adapted from [30]. Both Mach 6 and 7 nozzles are used in this work. The tunnel features a barrel of internal diameter $152mm$ and length $17.35m$. The barrel can be heated to $550K$, has a maximum pressure rating of $275bar$ (P_{fill}), and is separated from the nozzle plenum by an upstream facing plug valve [31]. The converging-diverging nozzles have an exit diameter of $350mm$ and produce a core flow of approximately $300mm$ diameter [32]. Several plateaus of steady state conditions are produced in the test section after the plug value opens, each lasting approximately $30ms$. The mean freestream conditions are found from a combination of the plenum pressure (K4, monitored for each shot) and previous characterization studies using Pitot pressure rakes and total temperature probes [30, 32]. While the total pressure is

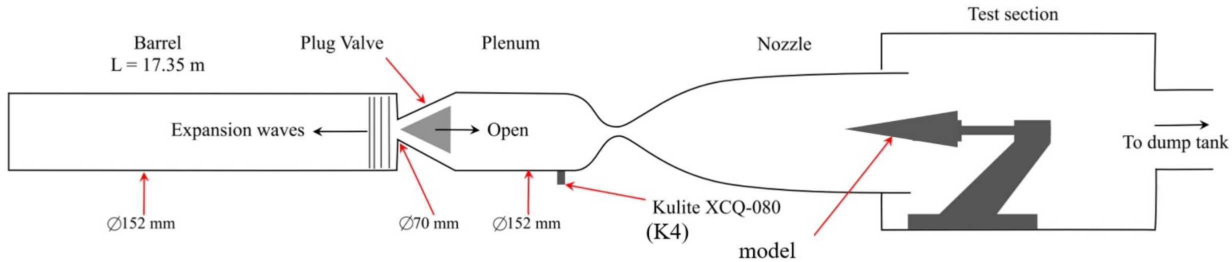

Fig. 1 Schematic of HDT facility.

P_{fill} (bar)	M_∞ (nominal) (-)	Plateau (-)	time (ms)	P_0 (MPa)	T_0 (K)	M_∞ (actual) (-)	U_∞ (m/s)	ρ_∞ (kg/m^3)	Re_{unit} ($10^6/m$)
65	6	1	55-65	5.6	475	6.15	918	0.190	44
		2	120-150	4.9	448	6.15	892	0.177	42
		3	205-235	4.3	440	6.15	884	0.158	38
	7	1	55-65	5.9	515	7.15	973	0.096	28
		2	120-150	5.5	465	7.15	922	0.099	31
		3	205-235	5.1	455	7.15	914	0.094	30
uncertainty				0.05	30	0.2	50	0.007	2

Table 1 Typical freestream conditions in HDT

steady for ~ $40ms$ during each plateau, the total temperature is much less steady during the first plateau [30]. Thus, when computing steady state averages we use a $10ms$ time period for plateau #1 and a $30ms$ time period for the other plateaus. These timings as well as the corresponding typical run conditions in this campaign are provided in Table 1. Previous freestream characterizations with Pitot probes found a significant drop in the post-shock turbulence intensity (P'_0/P_0 drops from 1.5% to 0.5%) from plateau #1 to plateaus #2 and #3 [32]. This variation provides a means of studying the effect of freestream noise on the transition process.

The model under investigation is a 7-degree half-angle (θ_c) cone at zero angle-of-attack with a base diameter of $146mm$ and a total length of $594.5mm$ when a sharp nose tip is installed. A simplified diagram of the model, coordinate axes, and locations of diagnostics is provided in Fig.2. It was used previously by Kerth et al. [22] for boundary layer transition studies and full details of the manufacturing, sensor locations and calibrations are provided here [23]. Interchangeable nose tips with radius $R_N = 0.05, 1.25, 3, 5$ & $9mm$ are swapped during the campaign to alter the size of the entropy layer on the model and explore the effects of nose bluntness on instabilities and transition. The x axis points in the direction of freestream flow and is coincident with the tunnel's centreline and the cone's axis of rotation. $x = 0$ corresponds to the apex of the cone with a sharp tip. The X_s axis follows surface streamlines with $X_s = 0$ at the stagnation point. X_s is related to x by

$$X_s = \frac{x}{\cos(\theta_c)} + R_N \left[\frac{\pi}{2} - \frac{1}{\sin(\theta_c)}\right]. \tag{1}$$

12 thin-film gauges (TFGs) and 19 PCB ultra high speed piezoelectric differential pressure transducers are flush mounted on the model surface to provide heat transfer and pressure data, respectively. The PCBs of interest are located on the bottom of the cone in the x-y plane bisecting the tunnel's span. The TFGs are offset from the PCBs by 15°. More detail on the sensors can be found here [23]. In addition to these surface measurements, schlieren images are acquired over a field-of-view (FOV) spanning ~ $150mm$ along the back of the cone. A conventional z-type schlieren setup is employed with a pulsed Cavitar C013 v1.0 Cavilux Smart UHS laser light source and a Phantom TMX 7510 camera. The knife edge is rotated by 7° such that the pixel intensity is proportional to the wall normal density gradient, $\partial\rho/\partial Y_s$ integrated along the line of sight. During each shot, 2000 images are recorded at $250kHz$ during plateau 2 (starting at $t = 130ms$).

The multipoint FLDI is positioned with its focus approximately $40mm$ below tunnel centreline and $65mm$ downstream

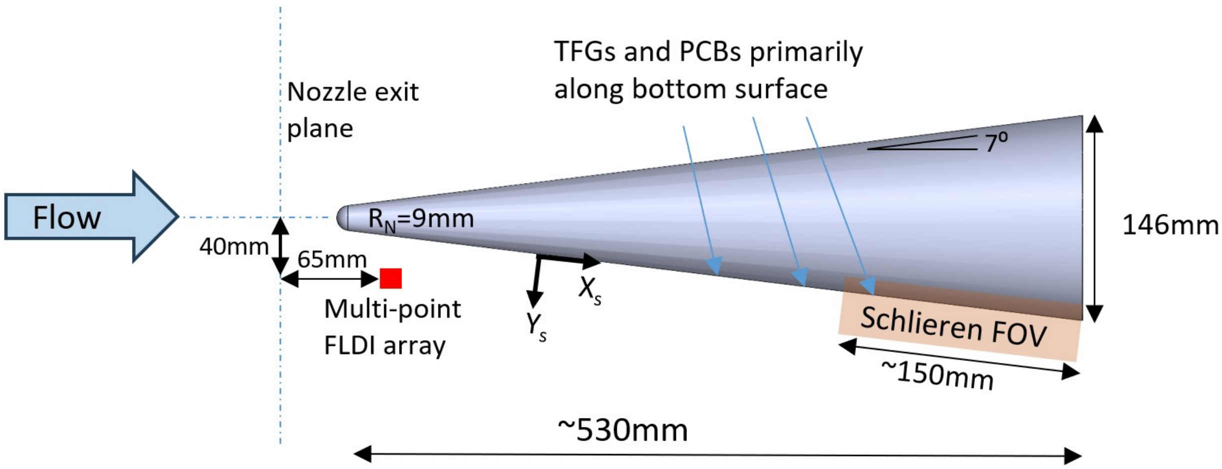

Fig. 2 Schematic of moderately blunt 7° cone, coordinate axes, and locations of optical diagnostic fields of view (FOV).

of the nozzle exit. The single-point FLDI employed in previous HDT experiments [23], which utilizes a Novanta Photonics Ventus solid state ($\lambda_0 = 671nm$) laser, is split into a 3x3 (9-point) grid with a diffractive optic element from HOLO/OR, as first suggested by Gragston et al. [33]. The nine signals are recorded using a custom photodiode array inspired by, and very similar to the array described by Davenport et al. [34]. The signals are recorded at $10MHz$ by two separate Pico Technology picoscopes (4444 and 4284). Fig.3.a shows a diagram of the foci at the tunnel's centre (x-y) plane and Fig.3.b shows a photo of the photodiode array and amplifier detection system. Prior to the campaign, a Thorlabs BC207VIS beam profiler camera was placed at the FLDI focus to determine the intra-probe and inter-probe beam spacings. Using the nomenclature of Ceruzzi and Cadou [25], the intra-probe beam spacing is $\Delta x_1 = 110 \pm 5\mu m$ and the inter-probe spacing is $\Delta x_2 = \Delta y_2 = 425 \pm 25\mu m$. The beam profiler camera was also translated along the optical axis to determine the beam's convergence/divergence angle and thus the effective beam radius parameter at the focus [25, 35] which was found to be $w_0 = 5.6 \pm 0.5\mu m$.

IV. Results

A. Transition location

The location of the start of transition is determined from the first TFG (in stream-wise order) which registers a heat flux above the laminar value in an effort to be consistent with the method used by Stetson et al. [18]. The TFG calibration procedure is described here [23]. The heat flux, $\dot{q}$, is reconstructed from the TFG signal with an impulse response based post-processing software [36] and the uncertainty is estimated as 25%. Stanton number, St, is computed as

$$St = \frac{\dot{q}}{\rho_e u_e c_p (T_r - T_w)} \tag{2}$$

where c_p is the specific heat capacity of dry air, T_w is the wall temperature (assumed constant at room temperature) and the recovery temperature, T_r, is expressed as

$$T_r = T_e \left[1 + r \left(\frac{\gamma + 1}{2} \right) M_e \right]. \tag{3}$$

The edge conditions with subscript e are estimated for each freestream condition using the Taylor-Maccoll equations [37–40], and the recovery factor, r is taken as 0.83 [41] for a Mach 6 & 7 laminar boundary layer. The laminar and turbulent Stanton numbers are determined from Eckert [42]. The TFG calibration constants are adjusted such that values measured during several large-bluntness, low Reynolds number runs ($R_N > 3mm$ and $Re_{unit} < 24 \times 10^6/m$) fall within the laminar curve.

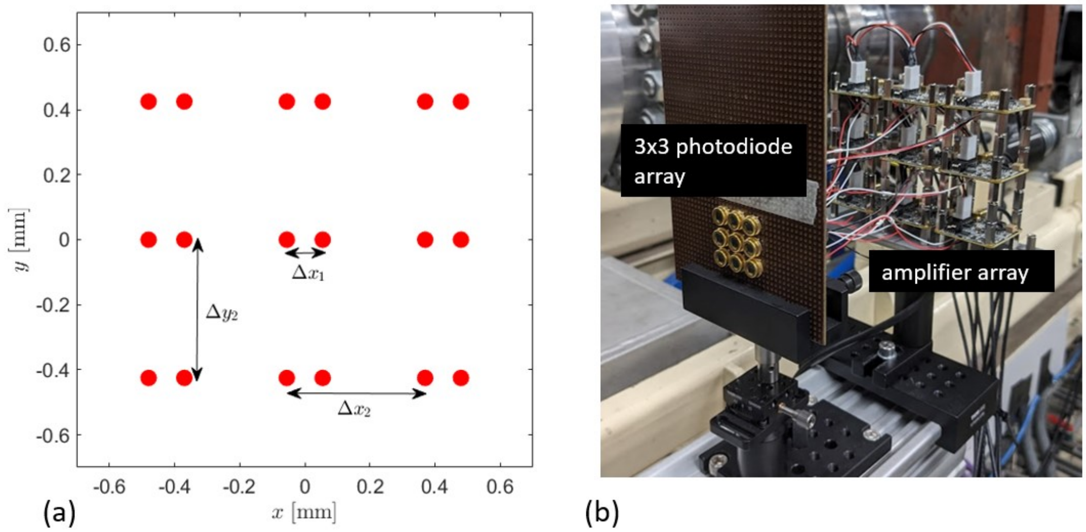

Fig. 3 (a) FLDI foci at tunnel centre-plane. (b) Photodiode array inspired by Davenport et al. [34].

Fig.4 shows the heat flux vs distance for several Mach 7 shots during plateau #1. As markers go from red to dark red to black the nose radius increases. Eckert's [42] laminar and turbulent heat fluxes are represented with thin solid and dashed lines, respectively. For the sharpest nose tip ($R_N = 0.05mm$, red circles), the heat flux is within the turbulent bounds for nearly all locations. This indicates the boundary layer has transitioned far forward on the cone. The start of transition is estimated as $X_T = 125 \pm 30mm$ for this case. As nose radius increases to $3mm$, the start of transition moves to the back of the cone, near $X_s = 470mm$. Notably, for $R_N = 5mm$ the heat flux distribution is similar, but slightly larger at the back of the cone to that at $R_N = 3mm$, indicating the transition front moved forward slightly. For $R_N = 9mm$ the heat flux stays within the laminar bounds along the entire cone. Heat flux distributions for Mach 7 plateau #2 and #3 are given in Appendix A. The key takeaway is that the transition front moves back from plateau #1 to #2 for all nose tips even though the Reynolds number increases slightly.

For the Mach 6 shots, we focus on the blunt nose tips of $R_N = 3$ & $9mm$ where the mechanisms which lead to transition are less well understood. Fig.5 shows the heat flux distribution for several Mach 6 shots during plateau #1. Note the unit Reynolds number for these shots, $44 \times 10^6/m$, is the largest achieved in this campaign. Under these conditions the blunter nose tip case ($R_N = 9mm$) transitions slightly before the sharper nose tip case ($R_N = 3mm$). Heat flux distributions for Mach 6 plateau #2 and #3 are provided in Appendix A.

The results of all tests are summarized in Fig.6 which plots transition Reynolds number, Re_{X_T}, against nosetip-radius Reynolds number, Re_{R_N}, with a comparison to similar experiments by Stetson [11] (Re-plotted on these axes by Jewell and Kimmel [10]). Re_{X_T} is computed by multiplying Re_{unit} by the start of transition in surface coordinate, X_T. Starting from the bottom left corner of Fig.6, the transition Reynolds number for sharp cones in HDT at Mach 7 is measured between 3 and 6 million with slightly larger values for plateau #2 & #3 compared to #1. As bluntness Reynolds number increases to 10^5, the transition Reynolds number increases up to 20 million for one shot in Mach 6 plateau #3. For Re_{R_N} between 10^5 and 4×10^5, Re_{X_T} remains relatively constant between 12 and 20 million. The general trend is in agreement with that observed by Stetson [11]. For almost every case Re_{X_T} increases with increasing number of plateau, with the most dramatic changes occurring between plateau #1 and #2. Significant scatter within plateau #1 is observed as well. As indicated on the plot, the change in slope near $Re_{R_N} = 10^5$ is hypothesized to be caused by a change in transition mechanism from second-mode waves to entropy-layer features [11, 17, 18]. Transition mechanisms are investigated in the next section and changes with plateau are addressed in Section IV.C.

B. Boundary layer instabilities

In this section we present schlieren images of the instabilities and flow features present on the model. For all shots, 2000 schlieren images are acquired at $250kHz$ during plateau #2. Prior to each shot, a flow-off background video is recorded with the same field of view and camera settings. For post-processing, this background video is subtracted from

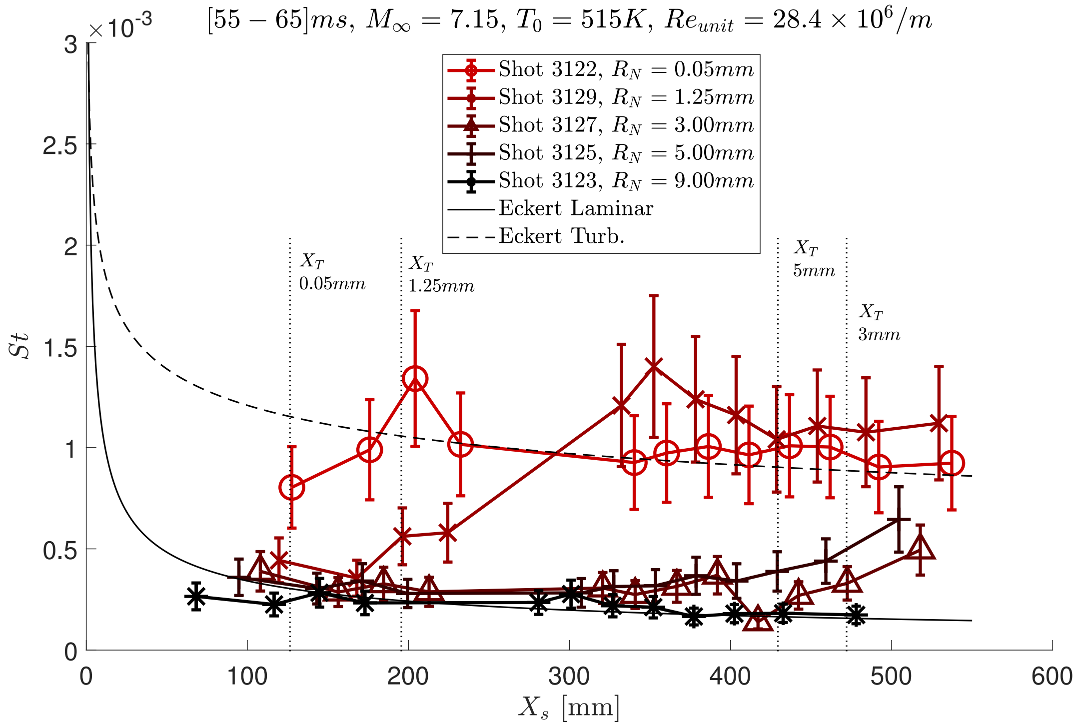

Fig. 4 Surface heat flux for Mach 7 freestream, plateau #1.

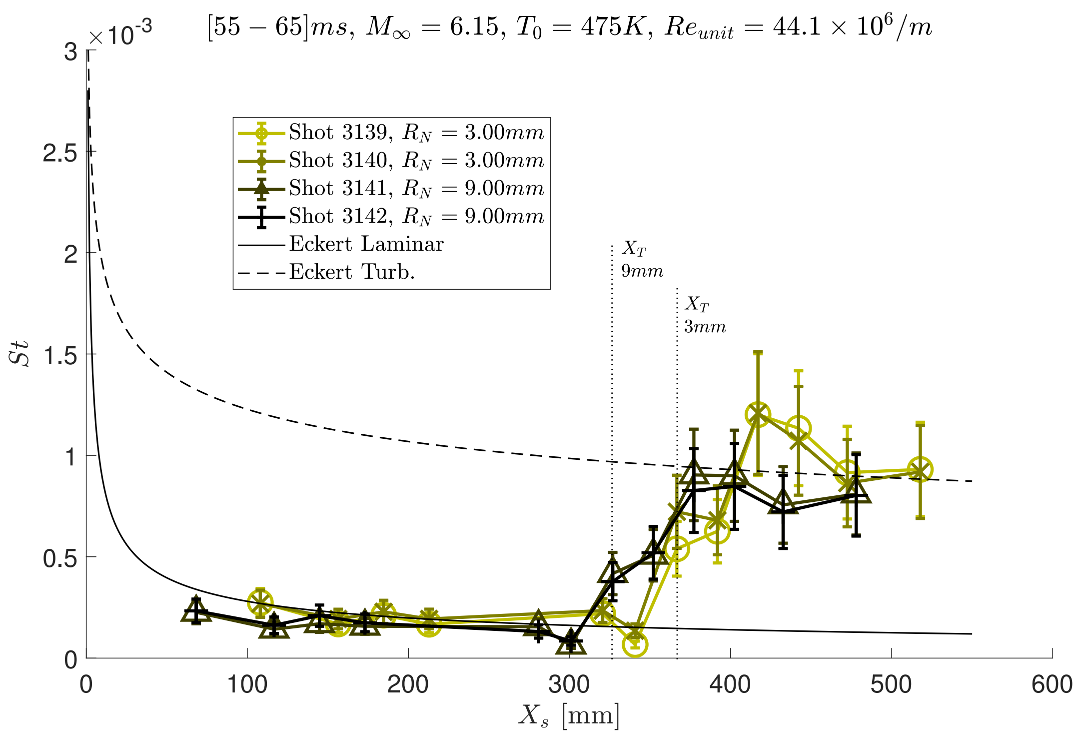

Fig. 5 Surface heat flux for Mach 6 freestream, plateau #1.

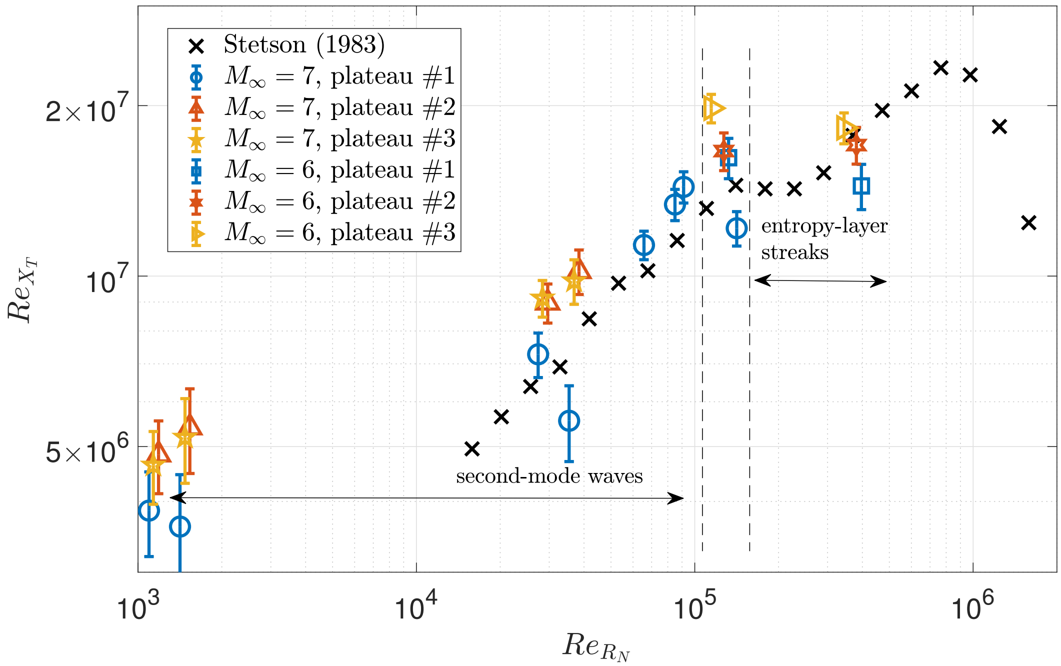

Fig. 6 Transition Reynolds number vs nose bluntness Reynolds number.

the flow-on video, frame by frame, to produce a background-subtracted video. Fig.7 shows a sequence of frames from shot 3137 where the nosetip radius is $3mm$ and $Re_{R_N} = 10^5$. The start of transition was not observed on the cone under these conditions. The boundary layer region is easy to identify with bright, large pixel intensity compared to the dark, black freestream above it and the boundary layer thickness, δ, is approximately $1.4mm$. A second-mode wave-packet is observed in these frames with rope-like appearance and a wavelength of approximately twice the boundary layer thickness [9]. Simultaneous with these images, power spectral density estimates of the PCB surface pressure fluctuations reveal a large peak in energy between 200-300kHz, also indicative of the 2nd-mode instability. A detailed analysis of the surface pressure is omitted here for the sake of brevity and will be included in future work. For all shots with $Re_{R_N} \leq 10^5$, evidence of the second-mode is observed in the schlieren images or surface pressure or both. This range of bluntness corresponds to the range where Re_{X_T} increases with Re_{R_N} (see Fig.6).

Fig.8 displays a sequence of schlieren images from shot 3133 where $R_N = 9mm$ and $Re_{R_N} = 2.8 \times 10^5$. The start of transition was also not observed on the cone under these conditions. The division between boundary layer and freestream is ambiguous with density gradients and structures present as high as $5mm$ above the surface. In the range of $Y_s = [2-4]mm$, coherent streaks and wisp-like structures convect through the flow. These structures are not observed near the surface, have longer streamwise spatial wavelengths, and arrive in seemingly irregular intervals compared to the second-mode wavepackets in Fig.7. These are the same types of entropy layer features observed by Grossir et al. [15], Kennedy et al. [17], and others [20]. The surface pressure measurements below these features reveal no clear frequency peaks and the heat fluxes remain at laminar values across the entire cone.

Finally, Fig.9 shows series of frames from shot 3141 where the nose tip radius is $9mm$ and the unit Reynolds number is large enough, $42.4 \times 10^6/m$, to cause the boundary layer to transition on the cone. A turbulent boundary layer is evident from the large bright, speckled region downstream in all frames. The start of transition, indicated with a white dashed line, is estimated to be just above $X_s = 400mm$ (see Fig.18). In the first (top) frame of Fig.9, between $X_s = [420-440]mm$, a wisp-like structure appears to crest above the boundary layer and bend back down into it. As time progresses (moving through image frames), that feature convects with the flow, highlighted by white dotted lines, and remains visible as the boundary layer becomes brighter, thicker, and turbulent. The feature does not 'break down' and disappear into the turbulent boundary layer as second-mode waves do [9]. Instead, the wisp/streak is still clearly visible at $X_s = 520mm$ in the final (bottom) frame. For all shots with $Re_{R_N} > 1.5 \times 10^5$ these wisps and streaks are observed above the boundary layer while second-mode waves are not observed inside the boundary layer. These

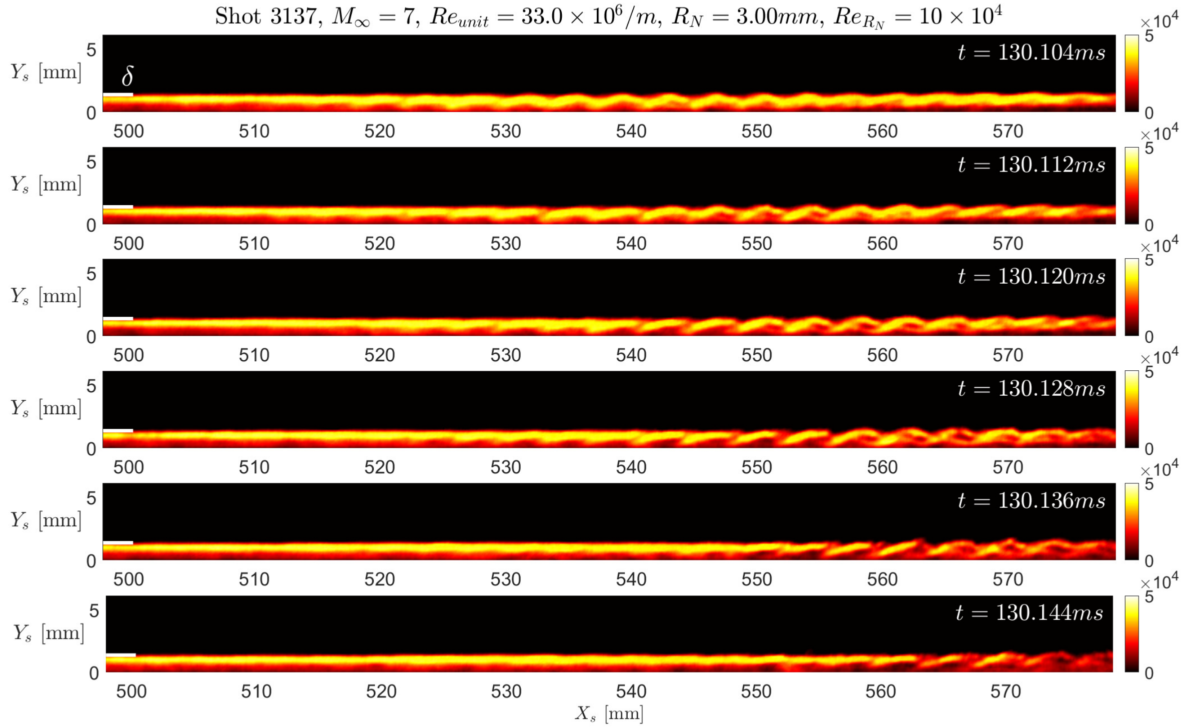

Fig. 7 Schlieren image sequence for shot 3137, $M_\infty = 7$, $Re_{unit} = 33 \times 10^6/m$, $R_N = 3mm$, $Re_{R_N} = 10 \times 10^4$.

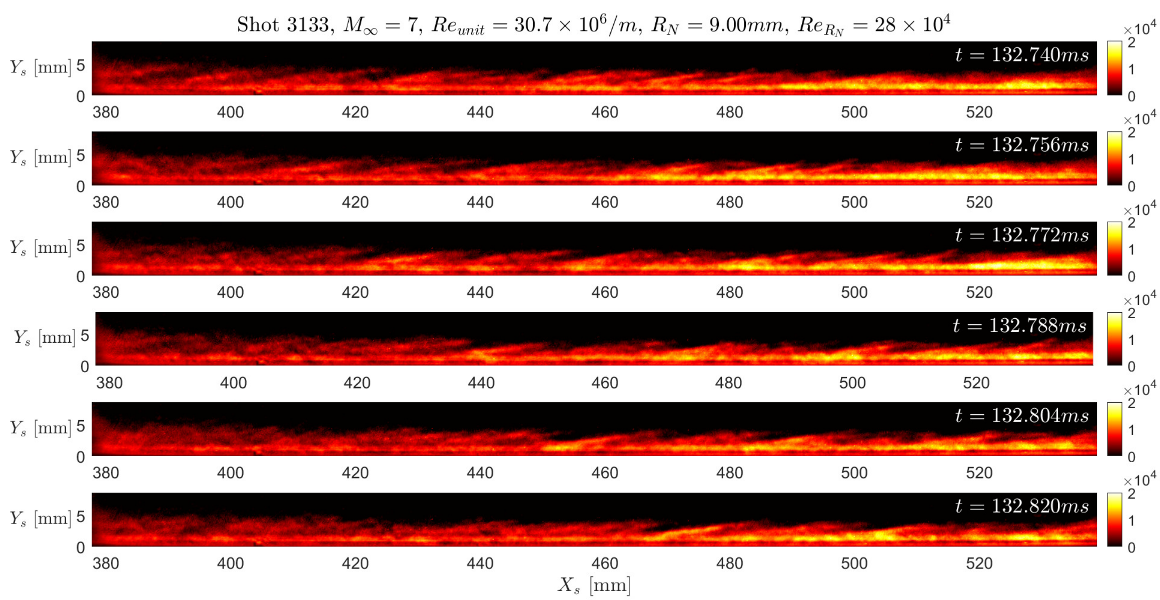

Fig. 8 Schlieren image sequence for shot 3133, $M_\infty = 7$, $Re_{unit} = 30.7 \times 10^6/m$, $R_N = 9mm$, $Re_{R_N} = 28 \times 10^4$.

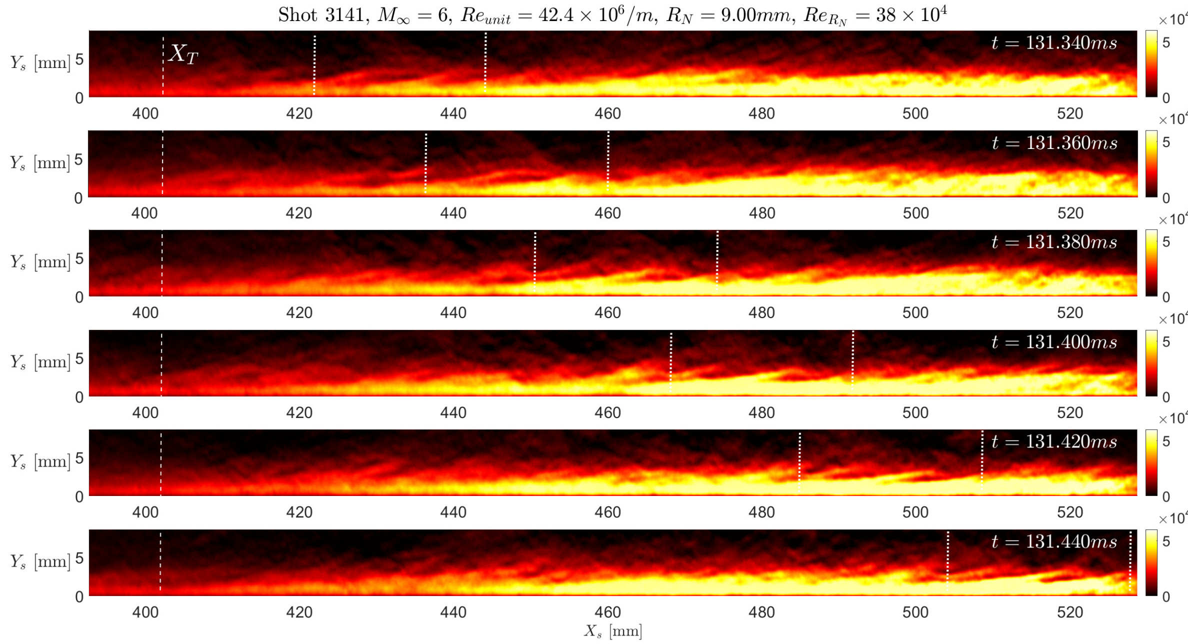

Fig. 9 Schlieren image sequence for shot 3141, $M_\infty = 6$, $Re_{unit} = 42.4 \times 10^6/m$, $R_N = 9mm$, $Re_{R_N} = 38 \times 10^4$.

bluntness Reynolds numbers correspond to the range where the transition Reynolds number remains constant with increasing bluntness. The combination of transition location trends and observable flow features suggest a change in transition mechanism occurs between $Re_{R_N} = [1 - 1.5] \times 10^5$.

C. Freestream disturbances

In this section we will address the freestream disturbances which are characterized using multi-point FLDI. First, a brief discussion of FLDI sensitivity, calibration, and post-processing is required to properly interpret the results. As suggested by Schmidt and Shepherd [43] and Settles and Fulghum [44], the FLDI's depth of focus increases for increasing disturbance wavelengths. This results in non-negligible signal contribution from large-wavelength disturbances in the nozzle shear layers. These disturbances are convecting at velocities less than or equal to the freestream, therefore their contribution to the FLDI signal is restricted to frequencies less than a cut-off. A method for estimating this cut-off frequency is proposed by Ceruzzi [45] and was recently employed by Gillespie et al. [27]. A simplified version of this method is employed here: Assuming disturbances are primarily flow-parallel and convecting with velocity (u_c) along the stream-wise axis (x), the variation in FLDI sensitivity along the optical axis (z) will only be a function of the transfer function, H_w, given by Eq.28 from Ceruzzi and Cadou [25]:

$$H_w = \exp\left(-\frac{\pi^2 w_0^2 f^2}{2u_c^2} - \frac{\lambda_0^2 f^2 z^2}{2w_0^2 u_c^2}\right). \tag{4}$$

Eq.4 is a Gaussian distribution with maximum value at $z = 0$. The integration length (L_{SR}) is found from the value of z at which the sensitivity falls to 1/e of it's maximum value. Thus, the integration length is expressed as

$$L_{SR} = \frac{\sqrt{8} w_0 u_c}{\lambda_0 f}, \tag{5}$$

and plotted in Fig.10 for $w_0 = 5.6\mu m$ and a convection velocity of $u_c = 1000m/s$. Fig.10 shows that the instrument's integration length is $\sim 120mm$ at $200kHz$ and grows exponentially as frequency decreases, reaching the entire length of the core flow ($300mm$) by $\sim 100kHz$. This suggest signals below $200kHz$ will represent large spatial averages and may

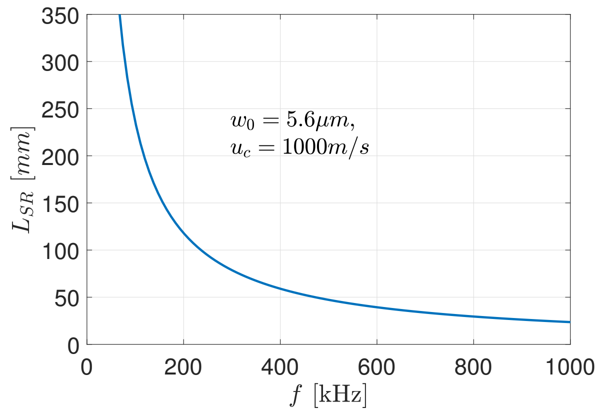

Fig. 10 FLDI integration length for a disturbance convecting at 1000m/s.

be contaminated by noise from the nozzle shear layers. Thus, in the following analysis we will restrict our focus to frequencies above $200kHz$.

The relationship between FLDI-measured voltage (V) and phase difference along the beam paths ($\Delta\phi$) is given by

$$V = V_0 + V_0 \cos(\Delta\phi + \phi_0) \tag{6}$$

where V_0 is the mean of the maximum and minimum voltage associated with total constructive and destructive interference, respectively, and ϕ_0 is the mean phase shift between the two beams [8, 25, 46]. V_0 and ϕ_0 are determined for each FLDI channel prior to each shot by mounting the beam-splitting Wollaston prism on a motorized translation stage and recording a range of voltages as the prism is translated along the axis of beam separation (x-axis in this work). During this calibration, six out of the nine FLDI channels were reliable while three yielded relatively small voltage ranges or non-existent signal. These malfunctions are believed to be caused by the photodiode amplifiers and future work will attempt to switch to a battery-biased photodiode array rather than one using amplifiers.

Phase differences are directly proportional to density gradients in the flow; the exact conversion is a complex function of the instrument and the flow field [47–49] and is left for future work. For the present analysis we define an 'FLDI-based turbulence intensity', $\Delta\phi/\rho_\infty$, which is proportional to the true density-based turbulence intensity. While the absolute magnitude of $\Delta\phi/\rho_\infty$ cannot be compared to other experiments, it can be compared run-to-run to measure the relative changes in density-based turbulence intensity within this campaign.

Fig.11 shows power spectral density (PSD) estimates of FLDI-based turbulence intensity for 3 shots. The PSDs are computed over each plateau using MATLAB's `pwelch` function with $100\mu s$ Hann windows and 50% overlap. A flow-off measurement is plotted as well (in dotted lines), taken just prior to each shot. All curves in Fig.11 represent the average of six PSDs from the six reliable FLDI channels. Very little variation in freestream spectra is observed between shots and plateaus; all spectra decay near a slope of $f^{-3.5}$ from $\sim [200 - 700]kHz$. This slope is in agreement with freestream measurements in many other facilities [50]. For frequencies above $700kHz$, spectra begin to coincide with the flow-off noise floor.

Turbulence intensity is computed from the spectra by integrating the the PSDs from $[195 - 605]kHz$, (using MATLAB's `trapz` function) and taking the square-root of the result. This operation is completed for each channel and the median value is plotted vs Reynolds number in Fig.12 along with a comparison to FLDI-based turbulence intensity measured by Gillespie et al. [27]. The data from Gillespie et al. [27] is re-scaled (by a factor of 3.6) such that a logarithmic fit to the data crosses through the measurements made in this work. The re-scaling accounts for the differences in FLDI transfer functions and mean turbulence intensities between the two facilities, and logarithmic fits are found to be good fits for turbulence intensity in many other facilities [51]. With the exception of shot 3137, where the turbulence intensity is $\sim$ 20% higher for plateau #1 vs #2 and #3, our data falls in line with the trend and scatter observed by Gillespie et al. [27] and no clear change with plateau is evident. This result was initially surprising, as the transition front consistently moved backwards with increasing plateau number. Additionally, previous studies found the post-shock pressure-based turbulence intensity measured with pitot probes to vary as much as 300% between plateau #1 and #2 [32]. Both discrepancies can be explained by bow shock receptivity, or bow shock transfer functions, which vary significantly with the inclination angle of the disturbance [52–54] and were not applied to the data reported previously

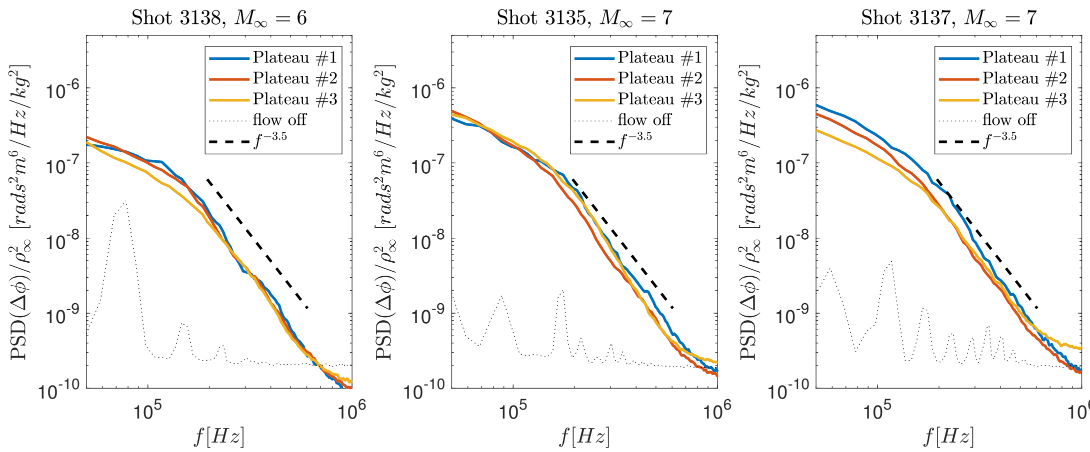

Fig. 11 FLDI-measured freestream disturbance spectra.

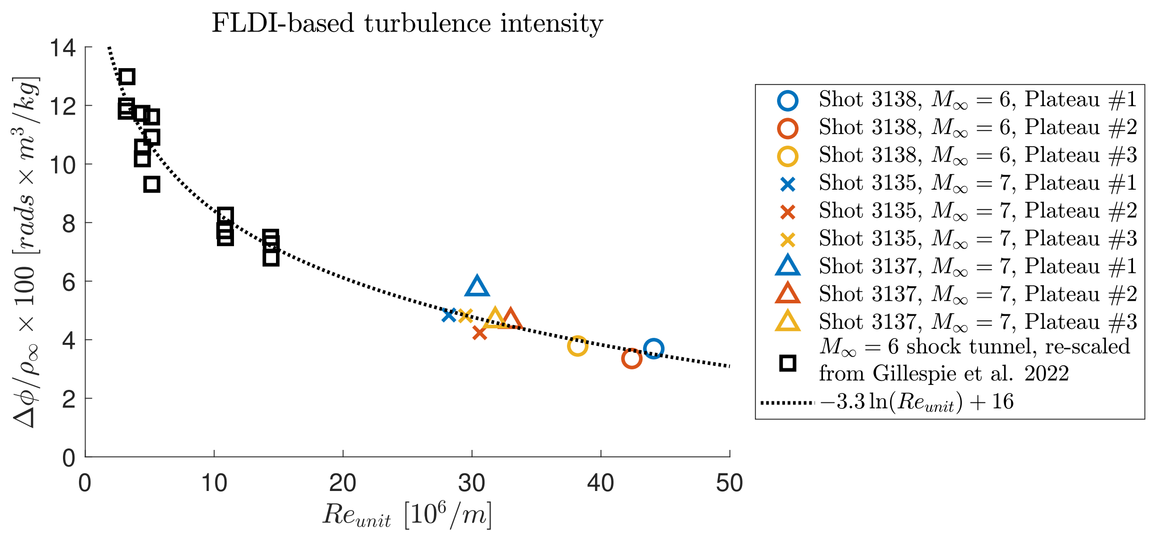

Fig. 12 FLDI-based (proportional to density-based) turbulence intensity over [195-605]kHz frequency band.

[32]. To investigate the inclination angles of the freestream disturbances, we will use correlations between signals in the two-dimensional FLDI array.

The normalized cross-correlation between FLDI channel i and j over sample period τ is computed using MATLAB's `xcorr` function and is expressed mathematically as

$$R_{ij}(\Delta t) = \int_0^\tau \frac{\Delta\phi_i(t)\Delta\phi_j(t+\Delta t)}{\sqrt{|\Delta\phi_i|^2}\sqrt{|\Delta\phi_j|^2}} dt. \tag{7}$$

Prior to this computation, each signal is band-passed between 200 and 600kHz to remove influence from the nozzle shear layers and the noise floor. The maximumly-correlated time lag between channels i and j can be interpreted as the relative time-of-arrival of correlated flow features and is expressed as

$$\Delta t_{ij} = \Delta t@\mathtt{max}[R_{ij}]. \tag{8}$$

The bulk streamwise convection velocity of disturbances, computed using stream-wise FLDI pairs separated by Δx_{ij}, is expressed as

$$u_c = \frac{\Delta x_{ij}}{\Delta t_{ij}}, \tag{9}$$

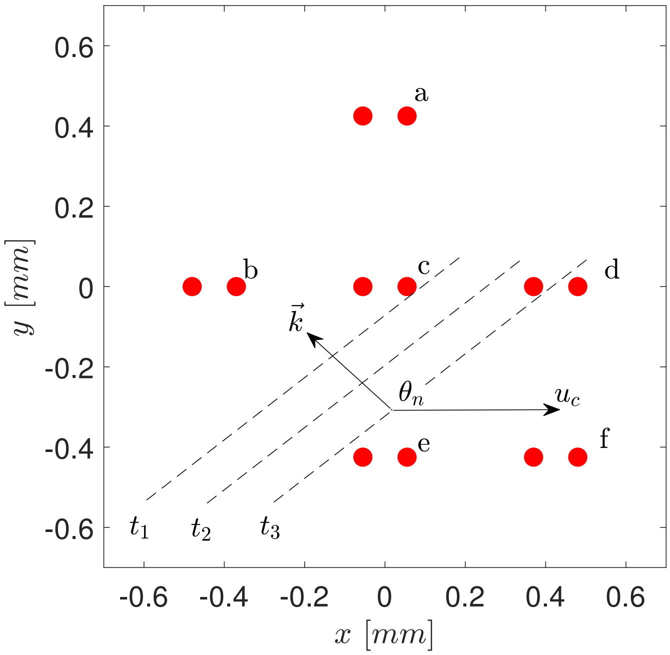

Fig. 13 Propagation of disturbance wavefront through FLDI probes.

and the absolute value of the inclination angle of disturbance waves, computed using span-wise FLDI pairs separated by Δx_{ij} and Δy_{ij}, is expressed as

$$|\theta_n| = \left| \tan^{-1} \left[\frac{v_c \Delta t_{ij} + \Delta y_{ij}}{u_c \Delta t_{ij} + \Delta x_{ij}} \right] \right| + 90^\circ. \tag{10}$$

The definition of θ_n is chosen to be consistent with the definitions used by others [50, 52–54] for backwards facing slow acoustic waves. The spanwise convection velocity, v_c, is assumed negligible in the following analysis. A physical interpretation of the streamwise convection velocity and disturbance inclination angle is illustrated in Fig.13 along with the six FLDI foci representing the channels which yielded a reliable signal.

Using the notation in Fig.13, the four FLDI pairs used for computing convection velocity are (b,c), (b,d), (c,d), & (e,f). The median of these four values is normalized by the respective freestream velocity for five shots & the first five plateaus and plotted in Fig.14 which also shows a comparison to data from Laufer [55] & Duan et al. [50] for pure acoustic waves radiated from turbulent boundary layers. The relative Mach number, M_r, between the freestream and acoustic waves is given by

$$M_r = \frac{U_\infty - u_c}{a_\infty}, \tag{11}$$

where $M_r = 1$, plotted with a solid line, represents the maximum velocity of a backwards-facing slow acoustic wave. For Mach 6, velocities are measured between 80-100% of the freestream while for Mach 7 velocities are 90-140% of the freestream. These values are slightly larger than $u_c/U_\infty \sim 0.7 - 0.8$ for pure acoustic waves radiating from turbulent boundary layers under similar conditions measured by Duan et al. [56]. This could be partially explained by the presence of non-acoustic disturbances convecting at the freestream velocity, such as entropy fluctuations originating from the plenum. However, no clear trend with plateau is evident and the unusually fast velocities and large scatter measured under Mach 7 conditions suggest uncertainty in the reported values is large.

Inclination angle is computed using Eq.10 with span-wise pairs (a,b), (a,c), (a,d), (b,e), (b,f), (c,e), (c,f), (d,e), & (d,f). The streamwise convection velocities, u_c, reported in Fig.14 are used in the calculation. Notably, the $\tan^{-1}$ term in Eq.10 is typically positive between pairs involving probes (e) & (f) and typically negative between pairs involving probe (a). This could be explained if FLDI probe (a) is more sensitive to acoustic waves radiating from the ceiling rather than the floor of the nozzle. The entire FLDI array is 40mm below the centreline ($\sim$ 23% of the nozzle radius) thus we expected the acoustic waves radiating from the floor of the nozzle with positive inclination angles to dominate

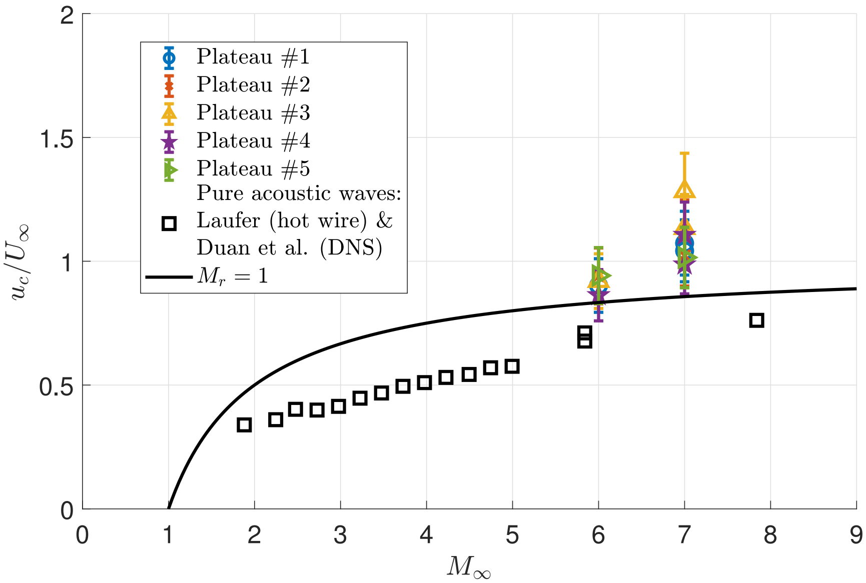

Fig. 14 Bulk disturbance convection velocity.

the signal. The finding suggest comprehensive modelling and bench testing with acoustic waves of known source is required for future work. To account for positive and negative θ_n we take the absolute value of the $\tan^{-1}$ term as is expressed in Eq.10. Fig.15 shows the median (over nine probe pairs) absolute inclination angle as well as a comparison to $[\theta_n]_{acoustic}$ converted the from bulk disturbance velocities of Duan et al. [50], Laufer [55] which are corrected by $-7°$ to account for the inclination of the Mach 6 nozzle contour at the source of the acoustic waves passing through the FLDI probes. This source location is found by tracing Mach lines backwards into the nozzle floor and ceiling where the local inclination angle is $-5°$ and $+9°$, respectively. Thus, the conversion from bulk disturbance velocity to inclination angle [53] for the historical data is:

$$[\theta_n]_{acoustic} = 180° - \cos^{-1}\left[\frac{1}{\left(1 - \frac{u_c}{U_\infty}\right) M_\infty}\right] - 7°. \tag{12}$$

Fig.15 also includes the angle of a freestream Mach wave, plotted with a solid black line. The inclination angles measured during plateau #1 ($\sim 130°$) are larger than those predicted for pure acoustic waves ($\sim 110° - 120°$) [50, 53] and the angles decrease with increasing plateau number, reaching minimum values of $|\theta_n| = [100° - 110°]$ for plateaus #3-#5. This supports the theory that a significant portion of disturbances in the early plateaus have wavefronts normal to the flow direction ($\theta_n = 180°$), biasing the average angle high. This behaviour could be explained by entropy fluctuations travelling along streamlines and originating from the plenum. The theory is further supported by previous freestream characterizations which indicated the total temperature is relatively unsteady during plateau #1 compared to the others [30].

To summarize this section, freestream disturbances in the [200-600]kHz range are characterized with a 6-point FLDI. Trends of disturbance amplitude with frequency and Reynolds number are in agreement with previous studies while trends with steady-state facility 'plateaus' are not. A method for estimating the average inclination angle of disturbances using cross-correlation between FLDI channels is presented and reveals a clear trend in angle with plateau number. We hypothesise this trend reflects a change in the relative contribution of entropic and acoustic modes which would explain the discrepancy between Pitot probe and FLDI measurements.

V. Summary and conclusions

This work presents an experimental investigation of boundary layer instabilities and transition over a $146mm$ base diameter, $7°$ half-angle cone at zero angle-of-attack in cold ($T_\infty < 60K$), hypersonic flow ($M_\infty = 6$ & 7). The nose tip

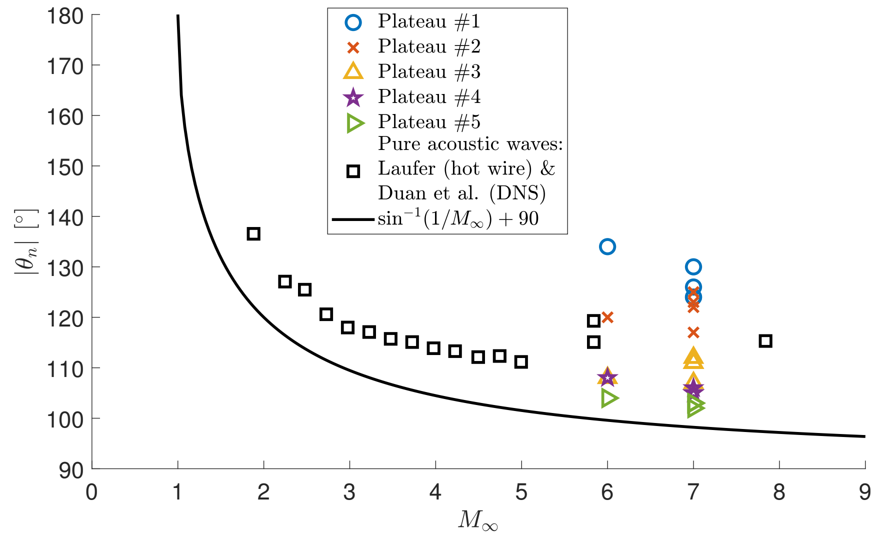

Fig. 15 Disturbance wave inclination angle.

radius is varied between $R_N = [0.05 - 9]mm$ with a focus on the 'moderately blunt' nose tips of $R_N \geq 3mm$. As the bluntness Reynolds number, Re_{R_N}, increases from $Re_{R_N} = 10^3$ to $Re_{R_N} = 10^5$, the transition Reynolds number, Re_{X_T}, increases from 3-6 million to 12-20 million. In this range, the mechanism which leads to transition is the amplification and breakdown of second-mode waves which are observed in both schlieren images and surface pressure measurements. Second-mode dominated transition has been studied extensively by others [6, 57]. For $10^5 < Re_{R_N} < 4 \times 10^5$, Re_{X_T} remains constant between 12-20 million. This may represent a change in the mechanism which leads to transition. For $Re_{R_N} > 1.5 \times 10^5$, Second-mode features are no longer observed, instead wisps and streaks with stream-wise wavelengths longer than the second-mode convect through the entropy layer, consistent with recent studies by others [15, 17, 20]. Schlieren images of the boundary layer transitioning to turbulence reveal the interaction of these entropy layer features with the boundary layer 'breakdown'.

The second part of this work presents a characterization of the freestream disturbance environment with multi-point FLDI which was performed simultaneously with the transition study. The freestream environment varies naturally with time (plateau) in this facility which causes the transition Reynolds number to increase with time, independent of bluntness. Density-based turbulence intensity does not vary significantly with time over the 200-600kHz frequency band, suggesting a more comprehensive characterization of the freestream environment is required. A consistent increase of the time-lag of the maximum cross-correlation between span-wise FLDI probes with plateau number suggests the average inclination angle of disturbances changes with time, and a method for computing this inclination angle is presented. Future bench testing and modelling are required to confirm if this method is physically valid. The inclination angles measured during plateaus #3-#5 are consistently smaller than those measured during plateaus #1 and #2. The findings suggest that the changes in transition location with plateau number are primarily driven by changes in receptivity to the waves of varying inclination, rather than changes in the overall freestream noise magnitudes. These receptivity transfer functions would also explain the discrepancies between FLDI-based turbulence intensity and post-shock Pitot probe turbulence intensity measured previously [32, 52, 53]. The inclination angle variation is physically explained by total temperature unsteadiness which increases the contribution of entropic disturbance modes relative to acoustic disturbance modes early in the facility run time [30]. The ability to directly measure inclination angles of disturbances represents significant progress in our ability to characterize the freestream environment in hypersonic facilities.

VI. Acknowledgments

The authors would like to acknowledge Tristen Crumpton for assistance with facility operation, Harry Kachika for machining parts of the model, Andreea Dabija for building the photodiode array, Chris Wheeler for assistance with schlieren alignment and data acquisition, Will Ivison for assistance with TFG data acquisition and post-processing, Chris Hambidge for facility management and operation, Jack Hillyer for assistance with the facilities data acquisition

and triggering system, and Stuart Laurence for suggesting the idea of these experiments.

References

[1] Shea, J., "Report of the Defense Science Board Task Force On National Aero-Space Plane (NASP) Program," Tech. rep., Defense Science Board, Washington, D.C., Nov. 1992.

[2] Van Driest, E. R., "The problem of aerodynamic heating," *Aeronautical Engineering Review*, Vol. 14, 1956, pp. 26–41.

[3] Reshotko, E., "Transition Issues at Hypersonic Speeds," *44th AIAA Aerospace Sciences Meeting and Exhibit*, American Institute of Aeronautics and Astronautics, Reno, Nevada, 2006. doi:10.2514/6.2006-707, URL https://arc.aiaa.org/doi/10.2514/6.2006-707.

[4] PATE, S. R., and SCHUELER, C. J., "Radiated aerodynamic noise effects on boundary-layer transition in supersonic and hypersonic wind tunnels." *AIAA Journal*, Vol. 7, No. 3, 1969, pp. 450–457. doi:10.2514/3.5128, URL https://doi.org/10.2514/3.5128, publisher: American Institute of Aeronautics and Astronautics _eprint: https://doi.org/10.2514/3.5128.

[5] Schneider, S. P., "Effects of High-Speed Tunnel Noise on Laminar-Turbulent Transition," *Journal of Spacecraft and Rockets*, Vol. 38, No. 3, 2001, pp. 323–333. doi:10.2514/2.3705, URL https://doi.org/10.2514/2.3705, publisher: American Institute of Aeronautics and Astronautics _eprint: https://doi.org/10.2514/2.3705.

[6] Marineau, E. C., "Prediction Methodology for Second-Mode-Dominated Boundary-Layer Transition in Wind Tunnels," *AIAA Journal*, Vol. 55, No. 2, 2017, pp. 484–499. doi:10.2514/1.J055061, URL https://arc.aiaa.org/doi/10.2514/1.J055061, publisher: American Institute of Aeronautics and Astronautics.

[7] Mack, L. M., "Linear Stability Theory and the Problem of Supersonic Boundary- Layer Transition," *AIAA Journal*, Vol. 13, No. 3, 1975, pp. 278–289. doi:10.2514/3.49693, URL https://arc.aiaa.org/doi/10.2514/3.49693, publisher: American Institute of Aeronautics and Astronautics.

[8] Parziale, N., "Slender-Body Hypervelocity Boundary-Layer Instability," Ph.D., California Institute of Technology, United States – California, 2013. URL https://www.proquest.com/docview/1500840637/abstract/9C1744DFBED943B6PQ/1, iSBN: 9781303709517.

[9] Laurence, S. J., Wagner, A., and Hannemann, K., "Experimental study of second-mode instability growth and breakdown in a hypersonic boundary layer using high-speed schlieren visualization," *Journal of Fluid Mechanics*, Vol. 797, 2016, pp. 471–503. doi:10.1017/jfm.2016.280, URL https://www.cambridge.org/core/journals/journal-of-fluid-mechanics/article/experimental-study-of-secondmode-instability-growth-and-breakdown-in-a-hypersonic-boundary-layer-using-highspeed-schlieren-visualization/1E77B7FEF1700ED4AD006CE1BDF8C867, publisher: Cambridge University Press.

[10] Jewell, J. S., and Kimmel, R. L., "Boundary-Layer Stability Analysis for Stetson's Mach 6 Blunt-Cone Experiments," *Journal of Spacecraft and Rockets*, Vol. 54, No. 1, 2017, pp. 258–265. doi:10.2514/1.A33619, URL https://arc.aiaa.org/doi/10.2514/1.A33619, publisher: American Institute of Aeronautics and Astronautics.

[11] Stetson, K., "Nosetip bluntness effects on cone frustum boundary layer transition in hypersonic flow," *16th Fluid and Plasmadynamics Conference*, American Institute of Aeronautics and Astronautics, 1983. doi:10.2514/6.1983-1763, URL https://arc.aiaa.org/doi/10.2514/6.1983-1763.

[12] Reda, D. C., "Review and Synthesis of Roughness-Dominated Transition Correlations for Reentry Applications," *Journal of Spacecraft and Rockets*, Vol. 39, No. 2, 2002, pp. 161–167. doi:10.2514/2.3803, URL https://doi.org/10.2514/2.3803, publisher: American Institute of Aeronautics and Astronautics _eprint: https://doi.org/10.2514/2.3803.

[13] Schneider, S. P., "Hypersonic laminar–turbulent transition on circular cones and scramjet forebodies," *Progress in Aerospace Sciences*, Vol. 40, No. 1, 2004, pp. 1–50. doi:10.1016/j.paerosci.2003.11.001, URL https://www.sciencedirect.com/science/article/pii/S037604210300112X.

[14] Kara, K., Balakumar, P., and Kandil, O. A., "Effects of Nose Bluntness on Hypersonic Boundary-Layer Receptivity and Stability over Cones," *AIAA Journal*, Vol. 49, No. 12, 2011, pp. 2593–2606. doi:10.2514/1.J050032, URL https://arc.aiaa.org/doi/10.2514/1.J050032.

[15] Grossir, G., Pinna, F., Bonucci, G., Regert, T., Rambaud, P., and Chazot, O., "Hypersonic Boundary Layer Transition on a 7 Degree Half-Angle Cone at Mach 10," *7th AIAA Theoretical Fluid Mechanics Conference*, American Institute of Aeronautics and Astronautics, 2014. doi:10.2514/6.2014-2779, URL https://arc.aiaa.org/doi/10.2514/6.2014-2779.

[16] Paredes, P., Choudhari, M. M., and Li, F., "Mechanism for frustum transition over blunt cones at hypersonic speeds," *Journal of Fluid Mechanics*, Vol. 894, 2020, p. A22. doi:10.1017/jfm.2020.261, URL https://www.cambridge.org/core/journals/journal-of-fluid-mechanics/article/mechanism-for-frustum-transition-over-blunt-cones-at-hypersonic-speeds/11B5BB8ABE3E6C4B58F6ED559C7BE69E, publisher: Cambridge University Press.

[17] Kennedy, R. E., Jewell, J. S., Paredes, P., and Laurence, S. J., "Characterization of instability mechanisms on sharp and blunt slender cones at Mach 6," *Journal of Fluid Mechanics*, Vol. 936, 2022, p. A39. doi:10.1017/jfm.2022.39, URL https://www.cambridge.org/core/journals/journal-of-fluid-mechanics/article/characterization-of-instability-mechanisms-on-sharp-and-blunt-slender-cones-at-mach-6/B535745D269754A7824F4E2E12E2AA10#, publisher: Cambridge University Press.

[18] Stetson, K., Thompson, E., Donaldson, J., and Siler, L., "Laminar boundary layer stability experiments on a cone at Mach 8. II-Blunt cone," *22nd Aerospace Sciences Meeting*, American Institute of Aeronautics and Astronautics, 1984. doi:10.2514/6.1984-6, URL https://arc.aiaa.org/doi/abs/10.2514/6.1984-6, _eprint: https://arc.aiaa.org/doi/pdf/10.2514/6.1984-6.

[19] Maslov, A., Mironov, S., Shiplyuk, A., Aniskin, V., Buntin, D., and Sidorenko, A., "Hypersonic flow stability experiments," *40th AIAA Aerospace Sciences Meeting & Exhibit*, American Institute of Aeronautics and Astronautics, Reno,NV,U.S.A., 2002. doi:10.2514/6.2002-153, URL https://arc.aiaa.org/doi/10.2514/6.2002-153.

[20] Paredes, P., Choudhari, M. M., Li, F., Jewell, J. S., Kimmel, R. L., Marineau, E. C., and Grossir, G., "Nose-Tip Bluntness Effects on Transition at Hypersonic Speeds," *Journal of Spacecraft and Rockets*, Vol. 56, No. 2, 2019, pp. 369–387. doi:10.2514/1.A34277, URL https://doi.org/10.2514/1.A34277, publisher: American Institute of Aeronautics and Astronautics _eprint: https://doi.org/10.2514/1.A34277.

[21] McGilvray, M., Doherty, L. J., Neely, A. J., Pearce, R., and Ireland, P., "The Oxford High Density Tunnel," *20th AIAA International Space Planes and Hypersonic Systems and Technologies Conference*, American Institute of Aeronautics and Astronautics, 2015. doi:10.2514/6.2015-3548, URL https://arc.aiaa.org/doi/abs/10.2514/6.2015-3548, _eprint: https://arc.aiaa.org/doi/pdf/10.2514/6.2015-3548.

[22] Kerth, P., Wylie, S., Ravichandran, R., and McGilvray, M., "Gas Injection into Second Mode Instability on a 7 degree Cone at Mach 7," *AIAA AVIATION 2022 Forum*, American Institute of Aeronautics and Astronautics, 2022. doi:10.2514/6.2022-3856, URL https://arc.aiaa.org/doi/abs/10.2514/6.2022-3856, _eprint: https://arc.aiaa.org/doi/pdf/10.2514/6.2022-3856.

[23] Kerth, P., "Effect of Transpiration Cooling on Boundary Layer Transition for Hypersonic Flight," Ph.D. thesis, University of Oxford, 2023.

[24] Gragston, M., Price, T. J., Davenport, K., Schmisseur, J. D., and Zhang, Z., "An *m* by *n* FLDI Array for Single-Shot Multipoint Disturbance Measurements in High-Speed Flows," *AIAA Scitech 2021 Forum*, American Institute of Aeronautics and Astronautics, VIRTUAL EVENT, 2021. doi:10.2514/6.2021-0599, URL https://arc.aiaa.org/doi/10.2514/6.2021-0599.

[25] Ceruzzi, A. P., and Cadou, C. P., "Interpreting single-point and two-point focused laser differential interferometry in a turbulent jet," *Experiments in Fluids*, Vol. 63, No. 7, 2022, p. 112. doi:10.1007/s00348-022-03459-w, URL https://link.springer.com/10.1007/s00348-022-03459-w.

[26] Parziale, N. J., Shepherd, J. E., and Hornung, H. G., "Free-stream density perturbations in a reflected-Shock tunnel," *Experiments in Fluids*, Vol. 55, No. 2, 2014. doi:10.1007/s00348-014-1665-0.

[27] Gillespie, G. I., Ceruzzi, A. P., and Laurence, S. J., "A multi-point focused laser differential interferometer for characterizing freestream disturbances in hypersonic wind tunnels," *Experiments in Fluids*, Vol. 63, No. 11, 2022, p. 180. doi:10.1007/s00348-022-03522-6, URL https://link.springer.com/10.1007/s00348-022-03522-6.

[28] Lawson, J. M., "Focused Laser Differential Interferometry," Ph.D. thesis, California Institute of Technology, 2021.

[29] Weisberger, J. M., Bathel, B. F., Herring, G. C., Buck, G. M., Jones, S. B., and Cavone, A. A., "Multi-point line focused laser differential interferometer for high-speed flow fluctuation measurements," *Applied Optics*, Vol. 59, No. 35, 2020, pp. 11180–11180. doi:10.1364/ao.411006.

[30] Hermann, T., McGilvray, M., Hambidge, C., and Doherty, L., "TOTAL TEMPERATURE MEASUREMENTS IN THE OXFORD HIGH DENSITY TUNNEL," *International Conference on Flight Vehicles, Aerothermodynamics and Re-entry Missions & Engineering*, Monopoli, Italy, 2019.

[31] Hillyer, J., Doherty, L., Hambidge, C., and McGilvray, M., "Extension of test time in Ludwieg tunnels," Heilbronn, Germany, 2022, p. 11.

[32] Wylie, S., "Hypersonic boundary layer instability measurements at low and high angles of attack," http://purl.org/dc/dcmitype/Text, University of Oxford, 2020. URL `https://ora.ox.ac.uk/objects/uuid:c6ab2886-c2a8-4d8b-b3e4-cfeecf397947`.

[33] Gragston, M., Price, T., Davenport, K., Zhang, Z., and Schmisseur, J. D., "Linear array focused-laser differential interferometry for single-shot multi-point flow disturbance measurements," *Optics Letters*, Vol. 46, No. 1, 2021, p. 154. doi:10.1364/OL.412495, URL `https://opg.optica.org/abstract.cfm?URI=ol-46-1-154`.

[34] Davenport, K., Ledbetter, S., Siddiqui, F., and Gragston, M. T., "Development of a Simple Compact Photodiode Array for Use with Linear Array-FLDI," *AIAA SCITECH 2023 Forum*, American Institute of Aeronautics and Astronautics, National Harbor, MD & Online, 2023. doi:10.2514/6.2023-1563, URL `https://arc.aiaa.org/doi/10.2514/6.2023-1563`.

[35] Siegman, A. E., *Lasers*, Univ. Science books, Mill Valley, Calif, 1986.

[36] Oldfield, M. L. G., "Impulse Response Processing of Transient Heat Transfer Gauge Signals," *Journal of Turbomachinery*, Vol. 130, No. 021023, 2008. doi:10.1115/1.2752188, URL `https://doi.org/10.1115/1.2752188`.

[37] Liepmann, H. W., and Roshko, A., *Elements of gasdynamics*, Galcit aeronautical series, Chapman & Hall, London, 1957.

[38] Anderson, J. D., *Modern compressible flow: with historical perspective*, McGraw-Hill series in mechanical engineering, McGraw-Hill, New York, 1982.

[39] Maccoll, J. W., and Taylor, G. I., "The conical shock wave formed by a cone moving at a high speed," *Proceedings of the Royal Society of London. Series A - Mathematical and Physical Sciences*, Vol. 159, No. 898, 1997, pp. 459–472. doi:10.1098/rspa.1937.0083, URL `https://royalsocietypublishing.org/doi/10.1098/rspa.1937.0083`, publisher: Royal Society.

[40] Taylor, G. I., and Maccoll, J. W., "The air pressure on a cone moving at high speeds.—I," *Proceedings of the Royal Society of London. Series A, Containing Papers of a Mathematical and Physical Character*, Vol. 139, No. 838, 1997, pp. 278–297. doi:10.1098/rspa.1933.0017, URL `https://royalsocietypublishing.org/doi/10.1098/rspa.1933.0017`, publisher: Royal Society.

[41] Anderson, J. D., *Hypersonic and high-temperature gas dynamics*, 2nd ed., AIAA education series, American Institute of Aeronautics and Astronautics, Reston, Va, 2006. OCLC: ocm68262944.

[42] Eckert, E. R. G., "SURVEY OF BOUNDARY LAYER HEAT TRANSFER AT HIGH VELOCITIES AND HIGH TEMPERATURES," Tech. Rep. WADC-TR-59-624, Minnesota. Univ., Minneapolis. Heat Transfer Lab., Apr. 1960. URL `https://www.osti.gov/biblio/4100883`.

[43] Schmidt, B. E., and Shepherd, J. E., "Analysis of focused laser differential interferometry," *Applied Optics*, 2015. doi: 10.1364/AO.54.008459.

[44] Settles, G. S., and Fulghum, M. R., "The Focusing Laser Differential Interferometer, an Instrument for Localized Turbulence Measurements in Refractive Flows," *Journal of Fluids Engineering, Transactions of the ASME*, Vol. 138, No. 10, 2016, pp. 1–10. doi:10.1115/1.4033960.

[45] Ceruzzi, A., "Development of Two-Point Focused Laser Differential Interferometry for Applications in High-Speed Wind Tunnels," Ph.D., University of Maryland, College Park, United States – Maryland, 2022. URL `https://www.proquest.com/docview/2681845978/abstract/C18090FBB3034797PQ/1`, iSBN: 9798834017769.

[46] Lawson, J. M., Neet, M. C., Grossman, I. J., and Austin, J. M., "Static and dynamic characterization of a focused laser differential interferometer," *Experiments in Fluids*, 2020. doi:10.2514/6.2019-2296, URL `https://doi.org/10.1007/s00348-020-03013-6`, publisher: Springer Berlin Heidelberg.

[47] Lawson, J., and Austin, J., "Recovering density disturbance spectra from FLDI. Part 2: Comparisons with previous methods," *Applied Optics*, 2023. doi:10.1364/AO.480354, URL `https://opg.optica.org/ao/abstract.cfm?doi=10.1364/AO.480354`.

[48] Lawson, J., and Austin, J., "Recovering density disturbance spectra from FLDI. Part 1," *Applied Optics*, 2023. doi: 10.1364/AO.480352, URL `https://opg.optica.org/ao/abstract.cfm?doi=10.1364/AO.480352`.

[49] Benitez, E. K., Borg, M. P., Luke Hill, J., Aultman, M. T., Duan, L., Running, C. L., and Jewell, J. S., "Quantitative focused laser differential interferometry with hypersonic turbulent boundary layers," *Applied Optics*, Vol. 61, No. 31, 2022, p. 9203. doi:10.1364/AO.465714, URL `https://opg.optica.org/abstract.cfm?URI=ao-61-31-9203`.

[50] Duan, L., Choudhari, M. M., Chou, A., Munoz, F., Radespiel, R., Schilden, T., Schröder, W., Marineau, E. C., Casper, K. M., Chaudhry, R. S., Candler, G. V., Gray, K. A., and Schneider, S. P., "Characterization of Freestream Disturbances in Conventional Hypersonic Wind Tunnels," *Journal of Spacecraft and Rockets*, Vol. 56, No. 2, 2019, pp. 357–368. doi:10.2514/1.A34290, URL https://doi.org/10.2514/1.A34290, publisher: American Institute of Aeronautics and Astronautics _eprint: https://doi.org/10.2514/1.A34290.

[51] Lafferty, J., and Norris, J., "Measurements of Fluctuating Pitot Pressure, "Tunnel Noise," in the AEDC Hypervelocity Wind Tunnel No. 9," *2007 U.S. Air Force T&E Days*, American Institute of Aeronautics and Astronautics, 2007. doi:10.2514/6.2007-1678, URL https://arc.aiaa.org/doi/10.2514/6.2007-1678.

[52] Chaudhry, R. S., Candler, G. V., Gray, K. A., and Schneider, S. P., "Computations of Measured Pitot-Probe Spectra using Angled Freestream Disturbances and Comparisons to Experiments," *AIAA Scitech 2019 Forum*, American Institute of Aeronautics and Astronautics, 2019. doi:10.2514/6.2019-2149, URL https://arc.aiaa.org/doi/10.2514/6.2019-2149.

[53] Schilden, T., and Schröder, W., "Inclined slow acoustic waves incident to stagnation point probes in supersonic flow," *Journal of Fluid Mechanics*, Vol. 866, 2019, pp. 567–597. doi:10.1017/jfm.2019.121, URL https://www.cambridge.org/core/journals/journal-of-fluid-mechanics/article/inclined-slow-acoustic-waves-incident-to-stagnation-point-probes-in-supersonic-flow/B64B85D6390883669B189505C6A61F67, publisher: Cambridge University Press.

[54] Lawson, J. M., Neet, M. C., Hofferth, J. W., and Austin, J. M., "Supersonic Freestream Density Fluctuations from Focused Laser Differential Interferometry and Pitot-Probe Measurements," *AIAA Journal*, 2022, pp. 1–14. doi:10.2514/1.J061432, URL https://arc.aiaa.org/doi/10.2514/1.J061432.

[55] Laufer, J., "Some Statistical Properties of the Pressure Field Radiated by a Turbulent Boundary Layer," *The Physics of Fluids*, Vol. 7, No. 8, 1964, pp. 1191–1197. doi:10.1063/1.1711360, URL https://doi.org/10.1063/1.1711360.

[56] Duan, L., Choudhari, M. M., and Zhang, C., "Pressure fluctuations induced by a hypersonic turbulent boundary layer," *Journal of Fluid Mechanics*, Vol. 804, 2016, pp. 578–607. doi:10.1017/jfm.2016.548, URL https://www.cambridge.org/core/journals/journal-of-fluid-mechanics/article/pressure-fluctuations-induced-by-a-hypersonic-turbulent-boundary-layer/0B2EB730CF31090295A19B1BE7103884, publisher: Cambridge University Press.

[57] Marineau, E. C., Grossir, G., Wagner, A., Leinemann, M., Radespiel, R., Tanno, H., Chynoweth, B. C., Schneider, S. P., Wagnild, R. M., and Casper, K. M., "Analysis of Second-Mode Amplitudes on Sharp Cones in Hypersonic Wind Tunnels," *Journal of Spacecraft and Rockets*, Vol. 56, No. 2, 2019, pp. 307–318. doi:10.2514/1.A34286, URL https://doi.org/10.2514/1.A34286, publisher: American Institute of Aeronautics and Astronautics _eprint: https://doi.org/10.2514/1.A34286.

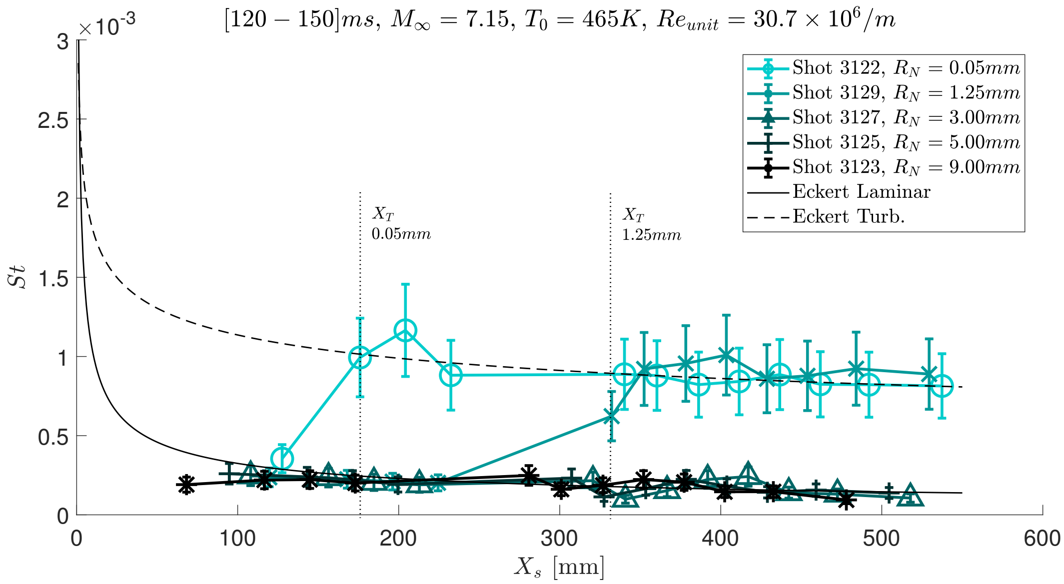

Fig. 16 Surface heat flux for Mach 7 freestream, plateau #2.

A. Heat flux distributions

Fig.16 shows the heat flux for the same shots as Fig.4 for plateau #2 rather than plateau #1. The key takeaway from Fig.16 is that the transition front has moved back from plateau #1 to #2 even though the Reynolds number has increased slightly. This behaviour is observed for all nose tips. For shots with $R_N \geq 3mm$ the boundary layer is fully laminar across the cone and thus the extent to which the transition front moved cannot be measured. Aside the $\sim 10\%$ increase in Reynolds number, other changes from plateau #1 to #2 include a drop in total temperature from 515K to 465K and any changes in the freestream disturbance environment which are addressed in Section IV.C. Fig.17 shows heat flux distributions for Mach 7 plateau #3 which are nearly identical to those measured in plateau #2.

The heat flux distributions for Mach 6 plateau #2 are plotted in Fig.18. Compared to plateau #1, the Reynolds number has dropped by 4% and the total temperature has dropped from $475K$ to $448K$. The transition front has moved back slightly ($\sim 5-10\%$) for the $3mm$ nosetip and more significantly ($\sim 10-25\%$) for the $9mm$ nosetip.

Fig.19 displays the heat flux for Mach 6 over plateau #3. The distributions are nearly identical regardless of nosetip with the only rise in heat flux measured at the very last TFG such that the blunter tip case starts to transition earlier than the sharper tip case. Compared to plateau #2, the Reynolds number has dropped by 10% in plateau #3 and the total temperature has not changed appreciably within the bounds of uncertainty ($\pm 30K$).

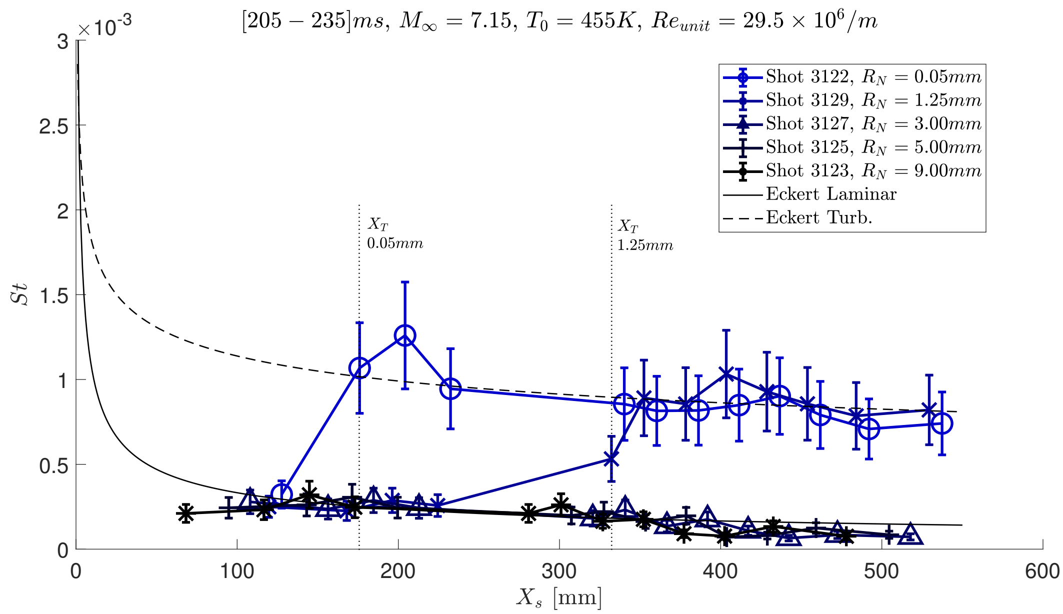

Fig. 17 Surface heat flux for Mach 7 freestream, plateau #3.

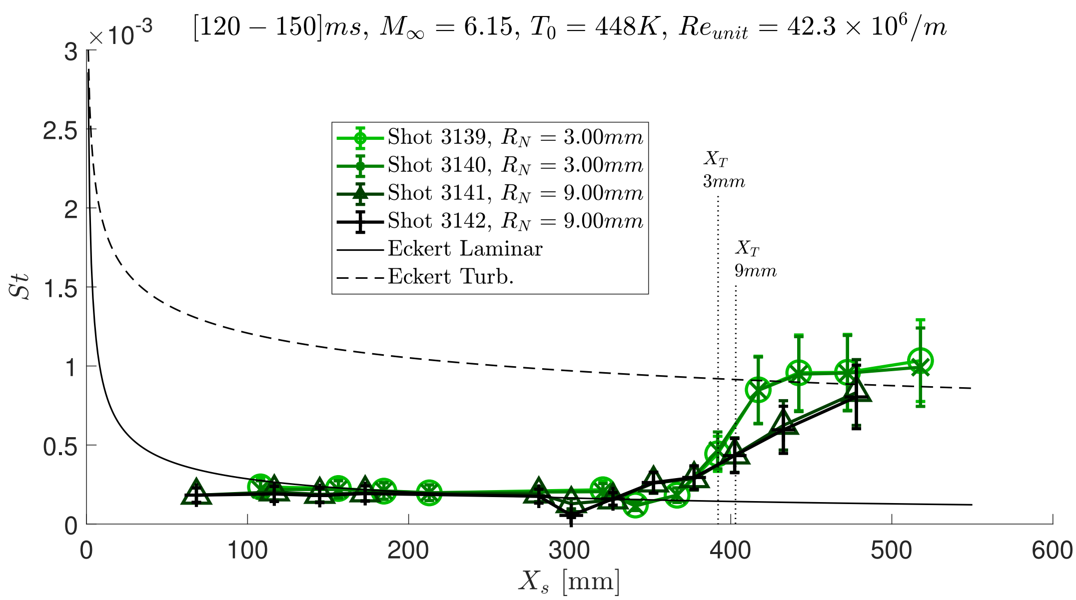

Fig. 18 Surface heat flux for Mach 6 freestream, plateau #2.

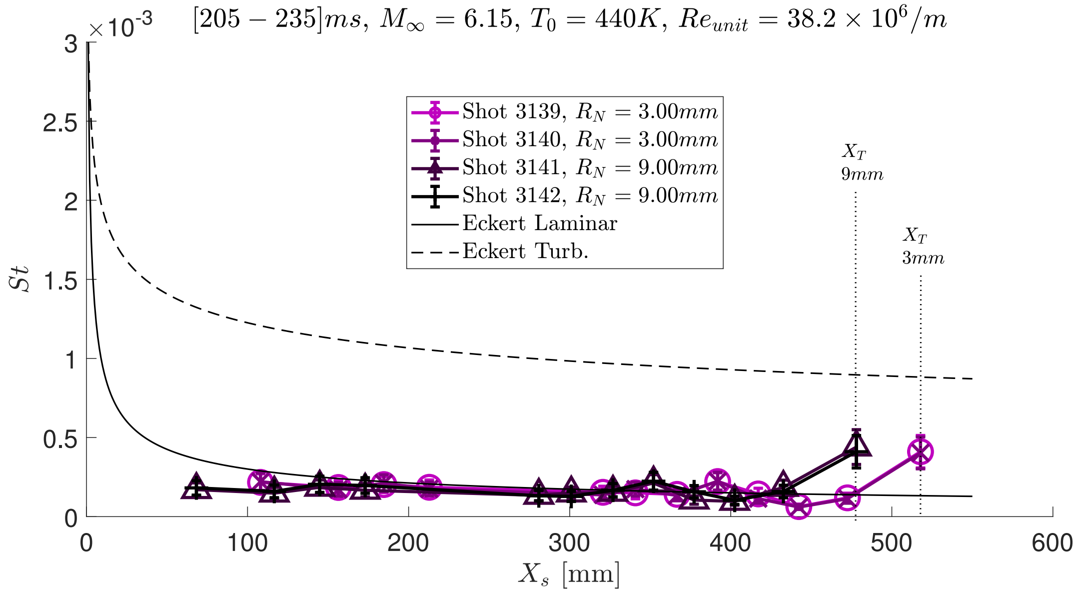

Fig. 19 Surface heat flux for Mach 6 freestream, plateau #3.